# Luminescence from amorphous silicon nanostructures

M. J. Estes* and G. Moddel
*Department of Electrical and Computer Engineering and the Optoelectronic Computing Systems Center, University of Colorado, Boulder, Colorado 80309-0425*
(Received 24 June 1996)

We present a model of size-dependent luminescence from *a*-Si:H and show that a blueshift of the luminescence energy and a general increase in luminescence quantum efficiency are predicted as structure size decreases. In contrast to bulk *a*-Si:H structures, highly confined *a*-Si:H exhibits visible luminescence peak energies and high radiative quantum efficiency at room temperature, which is insensitive to changes in temperature or defect density. We also predict a decrease in mobility and radiative decay time as structure size shrinks. We compare our results with observations of visible light emission from porous silicon. [S0163-1829(96)00844-2]

## I. INTRODUCTION

In a previous report,[1] we showed that size-dependent luminescence from disordered semiconductors may give insights into the mechanism of light emission from porous and nanostructured silicon. Indeed, efforts to understand this light emission in terms of a pure quantum confinement model in crystalline silicon have been complicated by observations of similar luminescence from nanostructured amorphous silicon. In particular, Bustarret *et al.* reported red-orange light emission from anodically etched and oxidized hydrogenated amorphous silicon-boron (*a*-Si:B:H) films very similar to that observed in identically anodized porous silicon wafers.[2,3] Lazarouk *et al.* found similar results in anodically oxidized *a*-Si:P:H pillar structures plasma deposited into porous alumina substrates.[4] We also found and reported on the visible light emission from anodized *p*-type *a*-Si:H and *a*-Si:C:H films.[5] Recently, Lu, Lockwood, and Baribeau[6] measured visible photoluminescence from *a*-Si/*a*-$SiO_2$ multilayers deposited by molecular-beam epitaxy. The peak energy of the light emission from these multilayers was shown to be size dependent, which the authors attributed to quantum confinement. However, because of the lack of crystallinity in these samples, we expect quantum confinement effects to be negligible.[7] Thus, another mechanism appears to be at work in this material.

Even in porous crystalline silicon, a significant number of observations point to a localized origin of the red-orange luminescence band in porous silicon. Specifically, Noguchi *et al.* observed strong photoluminescence (PL) from the topmost 1 $\mu$m of anodized porous silicon, a region that was determined to be primarily amorphous via transmission electron microscopy (TEM).[8] Perez *et al.* reported the observation of a strong Raman line at 480 $cm^{-1}$, which was attributed to amorphous silicon, in luminescing regions of anodized porous silicon.[9] Prokes, Freitas, and Searson also observed the strongest luminescence in the uppermost layers of anodized porous silicon and further correlated the redshift of the PL and intensity drop with thermal annealing with that of *a*-Si:H.[10] Hollingsworth *et al.* successfully fit the temperature dependence of the PL intensity from plasma-deposited and stain-etched porous silicon films with the exponential form observed in *a*-Si:H band-tail luminescence.[11] In addition, a number of researchers,[3,12–14] have reported a stretched exponential time decay of the PL from porous and nanoscale silicon. The stretched exponential decay, which arises from a wide distribution of decay times, is inherent in disordered semiconductors like *a*-Si:H.

Because of its low room-temperature luminescence quantum efficiency ($\sim 10^{-4}$) and $<$1.1-eV emission-peak energy,[15] *a*-Si:H might seem an unlikely candidate as the active luminescent material in porous silicon. Furthermore, several reports appear to correlate porous silicon luminescence energy with structure size, or at least porosity.[16,17] While there has been considerable research effort into possible quantum confinement effects in amorphous semiconductors, the overall effect appears to be quite small due to the generally localized nature of the carrier wave functions. Neglecting quantum size effects, conventional wisdom holds that there is no size dependence to the luminescence in disordered semiconductors. Higher emission energies, such as the 1.4–2.2-eV luminescence found in porous silicon, could be obtained by alloying amorphous silicon with oxygen,[18] nitrogen, or hydrogen. Alloying could even give a size dependence of sorts, since upon exposure to air, smaller silicon structures in the porous layer would have a greater fraction of oxide than larger structures. However, at least for plasma-deposited *a*-Si:O:N:H films, high-temperature annealing is required to obtained efficient room-temperature photoluminescence.[19] Thus we are faced with an apparent contradiction: evidence for localized transitions versus evidence for a size dependence, which implies delocalized transitions.

By applying a standard model of radiative recombination in *a*-Si:H to spatially confined *a*-Si:H nanostructures, however, we may resolve some of the apparent contradictions of porous silicon luminescence. In particular, we show that the luminescence may occur from localized states and still be size dependent. Using this model, we show that highly confined amorphous structures exhibit a blueshift and an increase in quantum efficiency of the radiative emission. While these effects are similar to the predictions of *quantum confinement* in a crystalline semiconductor, they are actually due to the statistics of *spatial confinement* in an amorphous semiconductor. We note that this concept is not new; Tiedje,

 © 1996 The American Physical Society

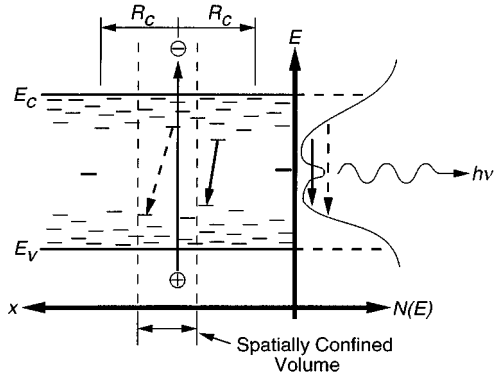


FIG. 1. Energy-band diagram of confined $a$-Si:H photoluminescence model. Photoexcited electrons and holes recombine within a capture radius $R_c$ via tunneling between localized tail states. By spatially limiting the recombination volume, the average luminescence energy and efficiency both increase.

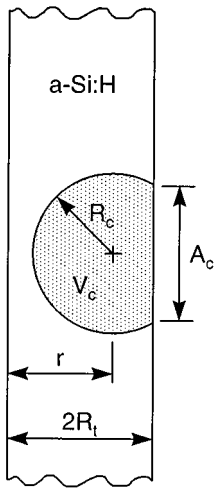


FIG. 2. Relationship between capture radius ($R_c$), capture volume ($V_c$), and surface capture area ($A_c$, edge view) of a capture sphere at position $r$ as truncated by a 2D $a$-Si:H slab of thickness $2R_t$.

Abeles, and Brooks used this model to successfully fit the observed layer thickness dependence of low-temperature photoluminescence in $a$-Ge:H/$a$-Si:H multilayer films,[20] and $a$-Si:H/$a$-Si:N:H multilayers.[21]

We consider here the luminescence of solid, isolated $a$-Si:H two-dimensional (2D) slabs, 1D round wires, and 0D spheres. This model, which is described in the next section, is a static (time-averaged) model that predicts photoluminescence quantum efficiency and emission spectra as functions of structure size and temperature. In the subsequent sections, we show predicted luminescence properties of confined $a$-Si:H nanostructures and also discuss in more qualitative terms the effects of confinement on carrier mobility and recombination dynamics.

## II. MODEL DESCRIPTION

### A. Background

Over the past two decades, researchers have extensively explored the luminescence properties of ''bulk'' $a$-Si:H.[15] Although the exact microphysical processes involved in the luminescence are still a matter of debate,[22] existing models of radiative recombination describe reasonably well the luminescence efficiency[15] and the spectral characteristics[23] of the 1.4-eV luminescence band. On the other hand, the luminescence properties of spatially confined amorphous silicon has only been briefly examined.[20,21] Here we consider the 2D slab case as well as the more highly confined 1D and 0D cases. In addition, we consider the temperature dependence of the predicted luminescence.

In this model, photogenerated carriers quickly thermalize to the lowest-energy states within some capture radius, $R_c$, before recombining. Radiative recombination then takes place via tunneling between deepest energy accessible conduction and valence-band states *without a Stokes shift*, as illustrated in Fig. 1. Thus, we will assume a rigid-band model. In contrast to Dunstan and Boulitrop,[23] we consider the entire density of states, including both exponential band-tail and quadratic band states as potential luminescing sites. We also assume that the density of states function is independent of size. For clusters of 10-Å diameter and larger this assumption should be reasonable as the density of states in amorphous semiconductors is determined primarily by nearest-neighbor interactions.[24] Radiative transitions to or from defect levels near midgap, such as the 0.9-eV low-temperature luminescence band in $a$-Si:H,[15] will not be considered here. As for the surfaces of the $a$-Si:H, we assume that there are additional nonradiative surface states from excess dangling bonds but no additional radiative surface states such as oxide defect centers[25] or luminescent molecular species like siloxenes.[26] For simplicity, we also assume that the Fermi energy level is constant throughout the structure and is located near midgap.

### B. Quantum efficiency

Nonradiative recombination occurs via tunneling to a nonradiative defect center when such a center is within the capture volume, $V_c$, defined by $R_c$, or on the surface capture area, $A_c$, truncating the capture sphere. In Fig. 2, we show the relationship between the capture radius, capture volume, and surface capture area. Thus, if $N_{\rm nr}$ is the volume nonradiative center density ($\rm cm^{-3}$) and $N_{\rm snr}$ is the surface nonradiative center density ($\rm cm^{-2}$) then the radiative quantum efficiency for a given electron-hole pair is given by[15]

$$\eta_i = \exp(-V_c N_{\rm nr})\exp(-A_c N_{\rm snr}). \tag{1}$$

This expression simply gives the probability of *not* finding a nonradiative recombination center within the capture volume and on the surface capture area. For an ensemble of electron-hole pairs, the net radiative efficiency is the spatial average of $\eta_i$ over the volume of the amorphous-silicon structure.[20] In this case, $V_c$ and $A_c$ are functions of position within the structure. For the 2D slabs, 1D wires, and 0D spheres that we consider, the average efficiencies are

$$\eta_{\rm 2D} = \frac{1}{R_t}\int_0^{R_t} \exp(-V_c(r)N_{\rm nr})\exp(-A_c(r)N_{\rm snr})dr, \tag{2a}$$

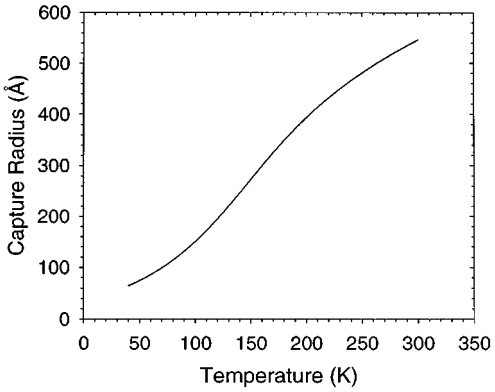


FIG. 3. Temperature dependence of the carrier capture radius, $R_c(T)$, computed from Eq. (4) with $N_{\rm nr}\sim 1\times 10^{16}$ cm$^{-3}$, $\eta_0\sim 0.998$, and $T_0\sim 23$ K.

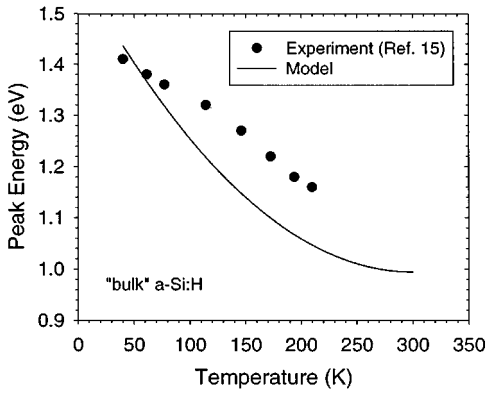


FIG. 4. Comparison of experimental (circles) and model (line) PL peak shift with temperature. Note qualitative agreement of redshift at higher temperatures but disagreement in shape of curve.

$$\eta_{\rm 1D}=\frac{2}{R_t^2}\int_0^{R_t} r\exp(-V_c(r)N_{\rm nr})\exp(-A_c(r)N_{\rm snr})dr, \tag{2b}$$

$$\eta_{\rm 0D}=\frac{3}{R_t^3}\int_0^{R_t} r^2\exp(-V_c(r)N_{\rm nr})\exp(-A_c(r)N_{\rm snr})dr \tag{2c}$$

where $R_t$ is the radius of the 0D sphere and 1D wire, and half the thickness of the 2D slab. The integration variable, $r$, is the position within the structure (radial distance from the center for the 0D and 1D cases and linear distance from one face for the 2D case).

### C. Capture radius and temperature dependence

The strong temperature dependence of the *a*-Si:H PL may be modeled by equating the expression for the *volume* quantum efficiency [Eq. (1) with $A_c=0$ and $V_c=4/3\pi R_c^3$] with an expression for the experimentally observed intensity temperature dependence in *a*-Si:H,[27]

$$\eta=\frac{1}{\left(\frac{1}{\eta_0}-1\right)\exp(T/T_0)}. \tag{3}$$

Here $T_0$ is an experimentally determined constant and $\eta_0$ is the low-temperature maximum quantum efficiency limit. The effective capture radius as a function of temperature is then found to be

$$R_c(T)=\left\{\frac{3}{4\pi N_{\rm nr}}\ln\left[\left(\frac{1}{\eta_0}-1\right)\exp(T/T_0)+1\right]\right\}^{1/3}. \tag{4}$$

We show a plot of $R_c(T)$ in Fig. 3 obtained by using nominal values for bulk *a*-Si:H (Ref. 27) of $\eta_0\sim 0.998$ and $T_0\sim 23$ K along with $N_{\rm nr}\sim 1\times 10^{16}$ cm$^{-3}$. At low temperatures, the capture radius is determined by the maximum probable tunneling distance, which is close to 70 Å at 40 K. At higher temperatures, though, carriers have enough thermal energy to diffuse a considerable distance before being trapped and recombining. From Eq. (4), we find the room-temperature capture radius in *a*-Si:H to be approximately 550 Å. When free carriers can move around and access a larger volume of amorphous silicon, they stand a greater chance of finding nonradiative recombination centers or very deep tail states. Thus, we should expect that at low temperatures or in highly confined amorphous silicon having well passivated surfaces, the radiative quantum efficiency and the luminescence energy should be higher than in the bulk material at room temperature. This idea is the basis of the model.

We note that this model oversimplifies the recombination process in *a*-Si:H, particularly at high temperatures. We have assumed that photoexcited electrons and holes diffuse independently. Thus, at high temperatures the pair may be separated well beyond practical tunneling distances for recombination. In reality, electrons and holes probably do not diffuse independently, and there probably is some correlation between deep states in the conduction- and valence-band tails. By its derivation, the model automatically accounts for the luminescence intensity temperature dependence. As we illustrate in Fig. 4, it also accounts for the experimentally observed decrease in luminescence energy with increasing temperature of *a*-Si:H,[15] although a discrepancy exists in the shapes of the modeled and experimental data. This poor correlation probably originates from oversimplification of the diffusion and tunneling processes. We have not taken into account the shift of *a*-Si:H band gap with temperature; however, this shift amounts to only $\sim$0.08 eV from 40 K up to 300 K.[28] For small capture volumes at low temperatures or in highly confined structures, this model should be reasonably accurate.

### D. Luminescence spectra

We use the method of Dunstan and Boulitrop[23] to compute the luminescence spectra. The amorphous-silicon density-of-states function (cm$^{-3}$ eV$^{-1}$) for the conduction band is given by

$$N_c(E)=\begin{cases} N_{\rm c0}\exp(E/E_{\rm c0}), & E\leqslant E_c\equiv 0 \\ N_{\rm c0}\left(\dfrac{2}{E_{\rm c0}}\right)^{1/2}(E-E_c')^{1/2}, & E>E_c, \end{cases} \tag{5}$$

where $E_c\equiv 0$ is the conduction-band energy at which the band and tail state densities are equal, $N_{\rm c0}$ is the effective

density of states ($cm^{-3}$) at $E_c$, $E$ is energy relative to $E_c$, $E_{c0}$ describes the slope of the band tail, and $E_c' = E_c - \frac{1}{2}E_{c0}$. $E_c'$ is determined by equating the density of states of the exponential band tail and the quadratic band at $E_c$. The valence band has a similar form for $N_v(E)$, where $E$ is valence-band energy relative to the energy $E_v \equiv 0$ at which the band and tail state densities are equal. In these equations, $E$ is not a global variable; it is in the frame of reference of either the conduction or valence band.

For an electron injected at an energy $\Delta E_c$ above $E_c$, the total number of accessible conduction-band states below $\Delta E_c$ and within the capture volume $V_c$ is given by

$$n_c = V_c \int_{-\infty}^{\Delta E_c} N_c(E)dE. \tag{6}$$

The probability density function $p_c(E)$ gives the probability that the lowest-energy conduction-band state within the capture volume, $V_c$, lies between $E$ and $E+dE$. It is then the probability that $n_c - 1$ states lie above the energy $E$ times the probability that the $n_c^{\text{th}}$ state is between $E$ and $E+dE$. Assuming that these $n$ states are independent, $p_c(E)$ is thus

$$p_c(E) = V_c N_c(E) \left[ \frac{\int_E^{\Delta E_c} N_c(E')dE'}{\int_{-\infty}^{\Delta E_c} N_c(E')dE'} \right]^{V_c \int_{-\infty}^{\Delta E_c} N_c(E')dE' - 1}. \tag{7}$$

A similar expression applies for the probability density function of highest-energy valence-band hole states, $p_v(E)$. The convolution of $p_c(E)$ and $p_v(E)$ (the two $E$ values are in different reference frames) yields the normalized photon flux luminescence spectrum, $P(h\nu)$, for a given electron-hole pair:

$$P(h\nu) = p_c(E) * p_v(E) = \int_{h\nu - \Delta E_v - E_g}^{\Delta E_c} p_c(E) p_v(h\nu - E_g - E)dE. \tag{8}$$

Here $E_g$ is the band-gap energy of the $a$-Si:H (defined as $E_g = E_c - E_v$) and $h\nu$ is the emitted photon energy. Since the luminescence spectrum is a function of capture volume, which in turn is a function of position within the amorphous structure, we must spatially average and multiply by photon energy to obtain the net intensity spectra for the three $a$-Si:H structures:

$$I_{2D}(h\nu) = \frac{h\nu}{R_t} \int_0^{R_t} \eta_i(r) P(h\nu, r)dr, \tag{9a}$$

$$I_{1D}(h\nu) = \frac{2h\nu}{R_t^2} \int_0^{R_t} r\,\eta_i(r) P(h\nu, r)dr, \tag{9b}$$

$$I_{0D}(h\nu) = \frac{3h\nu}{R_t^3} \int_0^{R_t} r^2 \eta_i(r) P(h\nu, r)dr. \tag{9c}$$

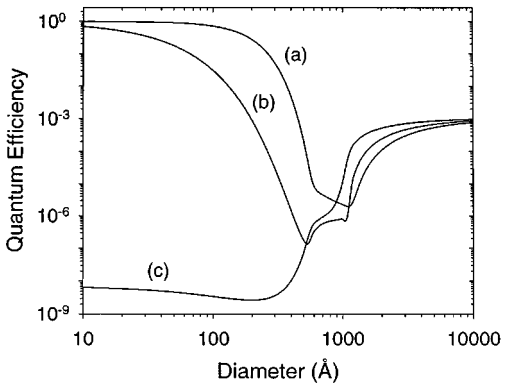


FIG. 5. Size dependence of the room-temperature internal radiative quantum efficiencies of (a) 0D, (b) 1D, and (c) 2D $a$-Si:H structures. The data were computed using volume and surface nonradiative recombination center densities of $1\times10^{16}$ $cm^{-3}$ and $1\times10^{11}$ $cm^{-2}$, respectively.

### E. Summary of model

As a way of summarizing the basic concepts of this model, let us do a thought experiment. Imagine that we have a large block of $a$-Si:H such that the block exhibits bulk absorption and luminescence characteristics. Now, let us cut up the block into many smaller, isolated pieces. We assume that all surface states that would give rise to absorption or radiation are passivated. Neglecting optical scattering, the excitation spectrum for the sum total of all the small blocks will be essentially the same as for the single large block since we assume that the density of states does not change with structure size. Luminescence, on the other hand, involves motion of carriers seeking out the lowest-energy recombination path within some distance, $R_c$, of the starting location. Therefore, while in the large block all the photoexcited carriers may recombine through only a few low-energy tail or defect states, in the smaller blocks carriers will find the lowest-energy paths within those smaller volumes. The average energy of this radiative recombination will be higher than for the single large block. Thus by cutting up the block we will see emission blueshift and absorption remain effectively unchanged.

## III. MODEL RESULTS

### A. Geometry

In this section, we present calculations of luminescence from the three $a$-Si:H structures. Our results show the effects of structure size between 10 Å and 1 $\mu$m diameter and temperature between 40 and 300 K on the predicted photoluminescence quantum efficiency and intensity spectra. We give expressions for the capture volume and surface capture area as functions of position for these three nanostructures in the Appendix.

### B. Quantum efficiency

In Fig. 5, we illustrate the effect of structure size on room-temperature quantum efficiency for the three $a$-Si:H structures with nominal values of the volume and surface nonradiative recombination center densities of $1\times10^{16}$ $cm^{-3}$

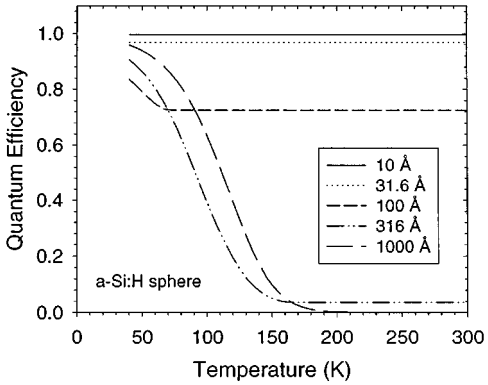


FIG. 6. Temperature dependence of the radiative quantum efficiencies of $a$-Si:H spheres of diameters from 10–1000 Å.

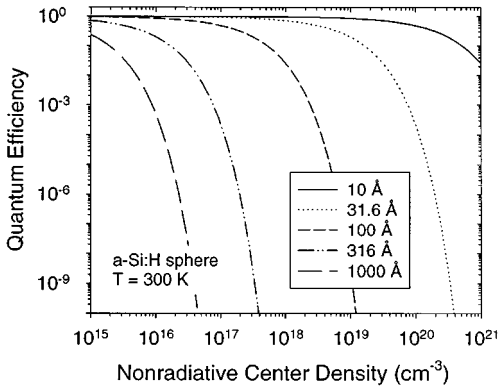


FIG. 7. Effect of nonradiative recombination center density on room-temperature radiative quantum efficiencies of $a$-Si:H spheres with diameters of 10–1000 Å. We have assumed that surface nonradiative center density varies as the $\frac{2}{3}$ power of the volume density.

and $1\times10^{11}$ cm$^{-2}$, respectively. The dip in efficiency between approximately 400 and 1000-Å diameter is due to the combination of relatively large surface area *and* relatively large volume of these structures so that carriers are exposed to a maximal number of nonradiative sites. The near unity quantum efficiency of the small 1D and 0D structures results simply from there being very few states, and hence a small probability of a nonradiative recombination center, within these volumes. The 2D structure, on the other hand, still has significant accessible surface area even for very thin layers and hence a much lower quantum efficiency. The predicted quantum efficiency is probably a bit too low, however, since we expect carrier mobility to be reduced by confinement, as we discuss in the Sec. IV.

At lower temperatures, the shorter capture radius results in a higher quantum efficiency for bulk structures, and so the difference in efficiency between large and small structures is lessened. In Fig. 6, we show the effect of temperature on quantum efficiency of various sizes of $a$-Si:H spheres. Greater spatial confinement results in reduced temperature dependence of the luminescence intensity.

We note that these data represent *internal* quantum efficiency only and do not reflect losses associated with light escaping the structure. In the case of porous media composed of small 1D and 0D $a$-Si:H structures, the effective-medium treatment applies for optical transmission and reflection. Thus, for highly porous material, the effective index of refraction is considerably lower than that for bulk $a$-Si:H and hence a greater fraction of the luminescent light may escape as the angle for total internal reflection is larger than for the bulk case. In conventional anodic porous silicon, for instance, von Behren *et al.*[29] measured an effective index of refraction of 2.0 from a 40% porosity layer and an index of only 1.3 from a 70% porosity layer. The nominal index of refraction of bulk crystalline silicon at 632 nm is 3.85. The net effect is that in highly porous material the external quantum efficiency approaches the internal quantum efficiency.

Both surface and bulk nonradiative recombination center densities affect the predicted quantum efficiency. The values used in Fig. 6, $1\times10^{16}$ cm$^{-3}$ and $1\times10^{11}$ cm$^{-2}$, are fairly small and indicative of very good $a$-Si:H. In highly defective, unhydrogenated amorphous silicon, on the other hand, the volume defect density approaches $10^{19}$ cm$^{-3}$, while the surface defect density may be as high as $10^{12}$–$10^{13}$ cm$^{-2}$. Quantum efficiency versus volume defect density for spheres of several sizes are shown in Fig. 7. In the figure, surface defect density is assumed to be volume defect density to the two thirds power. Because of lower carrier mobility in the unhydrogenated material, the room-temperature capture radius is smaller than for good $a$-Si:H. For simplicity, and as a worst case, we used the value of 550 Å for the capture radius in Fig. 7, independent of defect density. While high defect density effectively extinguishes bulk luminescence, greater confinement certainly lessens the effect. We note that while in many cases we have assumed defect density to be independent of structure size, in a real material system, such as porous silicon, stress and strain at the surface would likely cause an increased density of both surface and bulk nonradiative recombination centers leading to degraded quantum efficiency.

### C. Luminescence spectra and peak energy

In Fig. 8, we show predicted room-temperature luminescence intensity spectra for several $a$-Si:H spheres with diameters ranging from 10–1000 Å. These data were calculated using a mobility gap of $E_g$=1.7 eV, conduction- and

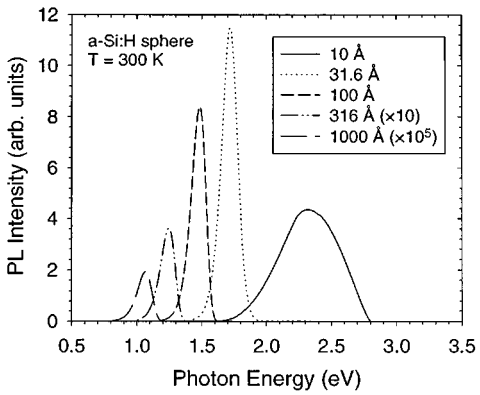


FIG. 8. Room-temperature luminescence spectra of several sizes of $a$-Si:H spheres.

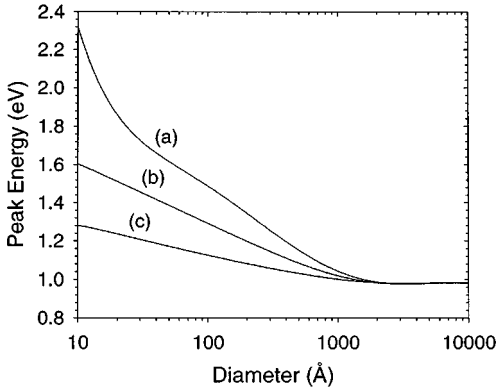


FIG. 9. Size dependence of the room-temperature photoluminescence peak energy for (a) 0D, (b) 1D, and (c) 2D $a$-Si:H structures.

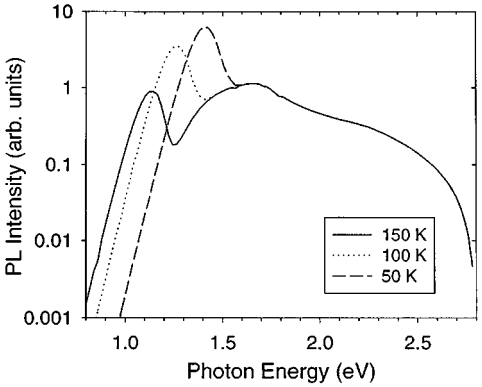


FIG. 10. Calculated PL spectra for a uniform size distribution of $a$-Si:H spheres with diameters from 10 Å to 1 $\mu$m and temperatures of 50, 100, and 150 K. At higher temperatures, the broad, ~1.65-eV PL peak is the predominant feature.

valence-band-tail slope energies of 0.026 and 0.043 eV, respectively, and conduction- and valence-band effective densities of states of $1\times10^{21}$ cm$^{-3}$. Respective volume and surface nonradiative center densities are $1\times10^{16}$ cm$^{-3}$ and $1\times10^{11}$ cm$^{-2}$. As the sphere diameter decreases, luminescence energy and intensity increase. The spectra from very small spheres have a larger width because the lowest-energy levels in these small structures may be parabolic band states. The spectra exhibit a linewidth of approximately 0.13–0.14 eV, which increases to more than 0.25 eV in spheres smaller than 20-Å diameter. By comparison, porous silicon linewidths are typically 0.3–0.4 eV. The broad, homogeneous linewidth predicted by this model results from the statistical distribution of states in $a$-Si:H. A distribution of structure sizes, which one might expect to find in porous silicon, would further broaden the peak.

In Fig. 9, we plot the peak energy of the luminescence intensity versus size for the three $a$-Si:H structures using the the same parameters as for the previous graph. To obtain the nominally 1.6–2.0 eV room-temperature luminescence observed in porous silicon, we would need $a$-Si:H spheres of approximately 10–50-Å diameter. Considering the observed structure sizes in luminescent porous silicon, this size range is reasonable. We note that the predicted room-temperature peak energy for the larger sized structures may be somewhat inaccurate due to oversimplification by the model; however, since we are interested only in the most highly confined structures, this inaccuracy should not lead to significant errors.

### D. Effect of size distribution

In the pure quantum confinement model, we would expect the optical emission spectra from a single crystallite to be very narrow. The broad emission from porous silicon would then be explained as being due to a distribution of crystallite sizes and shapes, all with different band gaps. In the confined amorphous-silicon model, though, we saw that a broad luminescence band (about half the width of a typical porous silicon peak) results from a single size and shape structure. Additional broadening and symmetry transformation takes place if we have a distribution of particle sizes. We show the temperature dependence of predicted luminescence spectra from a uniform size distribution of $a$-Si:H spheres with diameters from 10 Å to 1 $\mu$m in Fig. 10. The visible peak at ~1.65 eV is due to the very smallest spheres and is essentially independent of temperature. At low temperatures, the bulklike 1.4 eV $a$-Si:H peak appears along with the higher-energy peak. We clearly see an increased spectral width over the spectra in Fig. 8 with a full width at half maximum value of $>$0.4 eV. In addition, the effect of the sharp dip in efficiency for sizes between 500–1000 Å. (Fig. 6) is reflected in the spectra of Fig. 10 where two peaks are evident at lower temperatures.

## IV. DISCUSSION

### A. Spatial vs quantum confinement

While the effect of size-dependent luminescence from amorphous semiconductor nanostructures is similar to the effects of quantum confinement, it is instead due to the statistics of spatial confinement. In contrast to quantum confinement in a crystalline semiconductor, no coherent carrier wave-function interactions are assumed to take place in the amorphous semiconductor. Thus, the density of states remains unchanged by the confinement. Carriers are localized into band-tail states, whose density increases monotonically from midgap up into the band. It is the statistics of lowest-energy states within a volume that causes luminescence energy to increase as volume decreases. Unlike in quantum confined structures where the density of states is modified by confinement, the optical-absorption spectrum of confined amorphous silicon should *ideally* remain unchanged from the bulk case. However, we cannot completely neglect the effects of the environment confining the amorphous silicon. Both surface chemistry and surface stress will have an impact on the overall density of states. Silicon oxides or hydrides on the surface of the $a$-Si:H will create a surface with a wider band gap than the core. Stresses arising from surface oxidation may also generate additional bond strain and result in increased band-tail widths. Thus, for very small structures where the number of surface atoms is a significant fraction of the total number of atoms in the structure, the optical-absorption edge should shift toward the blue and become less abrupt. Correspondingly, the luminescence energy will

change as well. Our simple model does not take these effects into account quantitatively, but that should not detract from the validity of the spatial confinement concept.

### B. Mobility vs confinement

We also expect spatial confinement to have a subtle effect on carrier motion. In *a*-Si:H, carrier motion is thought to occur via tunneling between adjacent states that are at nearly the same energy.[30] Using this concept, the mobility edge may then be derived as the energy at which the density of states is high enough that the tunneling probability to an adjacent state approaches one. In the 3D case, that density is around $10^{21}$ cm$^{-3}$. In very thin 2D sheets or 1D wires, however, a higher density of states is required for the tunneling probability to approach one since carriers can only tunnel in two or one dimensions, respectively. By reducing the dimensions available for tunneling motion of a carrier at some fixed energy, we have reduced the probability of that carrier finding a percolation path along which to propagate through the amorphous-silicon network. The net effect is a reduction of carrier mobility and a widening of the mobility gap. Our model does not take this effect into account. Reduced carrier mobility in confined *a*-Si:H structures should further blueshift the luminescence beyond that predicted by this model. Assuming that the confining surfaces are well passivated, an increase in quantum efficiency should also be realized. Furthermore, an increase in the effective band gap of the amorphous silicon may also give excited carriers more opportunity to become trapped in radiative surface states as may arise from luminescent surface compounds such as siloxene.[26]

### C. Time dependence

In this luminescence model we have assumed that carriers recombine by tunneling between spatially separated conduction and valence states. The average tunneling time for an electron and hole separated by a distance $R$ is given by[15]

$$\tau = \tau_0 \exp(2R/R_0), \tag{10}$$

where $1/\tau_0$ is the tunneling attempt rate ($\sim 10^8$ sec$^{-1}$ for the radiative transition) and $R_0$ is the effective Bohr radius. According to Street, this expression is valid for $R > R_0$, where $R_0 \sim 10$ Å. A distribution of tunneling distances results in a distribution of decay times and, hence, the stretched-exponential luminescence decay observed in both amorphous and porous silicon.

By restricting $R$ through spatial confinement, the average luminescence decay time becomes shorter. If we estimate the average tunneling distance in an *a*-Si:H sphere to be roughly the sphere radius, we can plot the average decay time versus peak energy, as in Fig. 11 where we plot average luminescence decay time along with the luminescence peak energy versus sphere radius. As sphere size decreases, PL energy increases, tunneling distance decreases, and recombination time decreases. For the nominally 1.4–2.2-eV porous silicon peak energies, average decay times would range from about $10^{-5}$–$10^{-8}$ sec. Here the model differs somewhat from observations in porous silicon, where average luminescence decay times range from about $10^{-4}$–$10^{-6}$ sec.

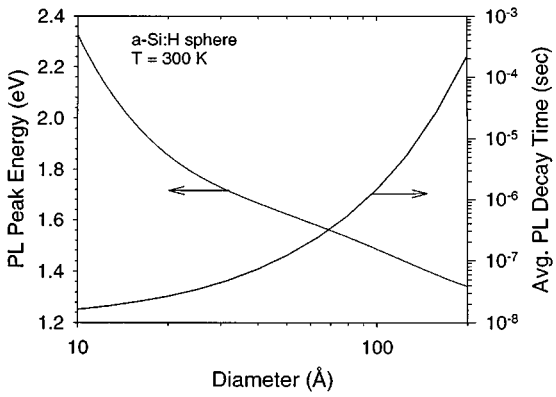


FIG. 11. Size dependence of PL peak energy (left axis) and average photoluminescence decay time (right axis) of *a*-Si:H spheres at room temperature.

## V. CONCLUSIONS

We have shown that under the assumptions of the *a*-Si:H luminescence model of Dunstan and Boulitrop, size-dependent luminescence is predicted for spatially confined *a*-Si:H nanostructures. In addition, emission efficiency also generally increases for structures less than ~100 Å in size, due to the decreased probability of finding a nonradiative recombination center. Highly confined 0D spheres can tolerate large volume defect densities $>10^{20}$ cm$^{-3}$ without a considerable loss in quantum efficiency. Luminescence peak energies in excess of 2 eV are possible in *a*-Si:H spheres with diameters <20 Å. The luminescence spectra exhibit homogeneous linewidths of ~0.14 eV in large structures to >0.25 eV in spheres <20 Å diameter. The effect of a distribution of structure sizes is an increase in the spectral width. Other, more subtle effects may be predicted for highly confined *a*-Si:H structures, such as a decrease in the luminescence decay time and an effective widening of the *a*-Si:H mobility gap. Effective band-gap widening through reduced carrier mobility, which this model does not account for, should also cause a blueshift of the luminescence energy.

## ACKNOWLEDGMENTS

We acknowledge financial support from the Materials Research Group and the Colorado Advanced Technology Institute. M. Estes gratefully acknowledges the support of the Air Force Institute of Technology. We thank J. Pankove, A. Gallagher, K. Douglas, and the members of the Thin Films Group for many useful discussions.

## APPENDIX

The expressions for capture volume, $V_c$, and surface capture area, $A_c$, as functions of position within 2D slabs, 1D wires, and 0D spheres are given here without derivation for a capture radius of $R_c$, a structure radius (or 2D slab half width) of $R_t$, and a center-to-center separation (or distance from left edge of 2D slab) of $r$.

**1. 2D planar slabs**

$$V_c=\begin{cases}\frac{4}{3}\pi R_c^3, & R_t\geqslant R_c,\ R_c\leqslant r\leqslant R_t-R_c\\ \pi[(R_c^2-r^2)(r+R_c)+r(r+R_c)^2-\frac{1}{3}(r+R_c)^3], & R_t\geqslant R_c,\ r<R_c\\ \pi\left[\begin{array}{l}(R_c^2-r^2)(2R_t-r+R_c)+\\ r\{4R_t^2-(r-R_c)^2-\frac{1}{3}[4R_t^3-(r-R_c)^3]\}\end{array}\right], & R_t\geqslant R_c,\ r>R_t-R_c\\ \pi[2(R_c^2-r^2)R_t+4rR_t^2-\frac{8}{3}R_t^3], & R_t<R_c,\ R_t-R_c\leqslant r\leqslant R_c\\ \pi\left[\begin{array}{l}(R_c^2-r^2)(2R_t-r+R_c)+\\ r\{4R_t^2-(r-R_c)^2-\frac{1}{3}[4R_t^3-(r-R_c)^3]\}\end{array}\right], & R_t<R_c,\ r>R_c\\ \pi[(R_c^2-r^2)(r+R_c)+r(r+R_c)^2-\frac{1}{3}(r+R_c)^3], & R_t<R_c,\ r<R_t-R_c\end{cases}$$

$$A_c=\begin{cases}0, & R_t\geqslant R_c,\ R_c\leqslant r\leqslant R_t-R_c\\ \pi(R_c^2-r^2), & R_t\geqslant R_c,\ r<R_c\\ \pi[R_c^2-(2R_t-r)^2], & R_t\geqslant R_c,\ r>R_t-R_c\\ \pi[2R_c^2-r^2-(2R_t-r)^2], & R_t<R_c,\ R_t-R_c\leqslant r\leqslant R_c\\ \pi[R_c^2-(2R_t-r)^2], & R_t<R_c,\ r>R_c\\ \pi(R_c^2-r^2), & R_t<R_c,\ r<R_t-R_c.\end{cases}\tag{A2}$$

**2. 1D cylindrical wires**

$$V_c=\begin{cases}\frac{4}{3}\pi R_c^2, & R_t\geqslant R_c,\ r\leqslant R_t-R_c\\ 2\int_0^{R_c}A_i(\sqrt{R_c^2-z^2},R_t,r)\,dz, & R_t\geqslant R_c,\ r>R_t-R_c\\ 2\int_0^{R_c}A_i(\sqrt{R_c^2-z^2},R_t,r)\,dz, & R_t<R_c,\end{cases}\tag{A3}$$

where $A_i(r_1,r_2,d)$ is the area of intersection of two circles of radii $r_1$ and $r_2$ separated by a distance $d$ and is defined by

$$A_i(r_1,r_2,d)=\begin{cases}\left\{\begin{array}{l}-(d+x_i)\sqrt{r_1^2-(d+x_i)^2}\\ +r_2^2\left[\frac{\pi}{2}-\sin^{-1}\left(\frac{d-x_i}{r_1}\right)\right]\\ -x_i\sqrt{r_2^2-x_i^2}+r_2^2\left[\frac{\pi}{2}-\sin^{-1}\left(\frac{x_i}{r_2}\right)\right]\end{array}\right\}, & \begin{array}{l}r_2\geqslant r_1,\\ r_2-r_1<d<r_2+r_1\end{array}\\ 0, & r_2\geqslant r_1,\ d\geqslant r_2+r_1\\ \pi r_1^2, & r_2\geqslant r_1,\ d\leqslant r_2-r_1\\ \left\{\begin{array}{l}-(d+x_i)\sqrt{r_1^2-(d+x_i)^2}\\ +r_1^2\left[\frac{\pi}{2}-\sin^{-1}\left(\frac{d-x_i}{r_1}\right)\right]\\ -x_i\sqrt{r_2^2-x_i^2}+r_2^2\left[\frac{\pi}{2}-\sin^{-1}\left(\frac{x_i}{r_2}\right)\right]\end{array}\right\}, & \begin{array}{l}r_2<r_1,\\ r_1-r_2<d<r_1+r_2\end{array}\\ 0, & r_2<r_1,\ d\geqslant r_1+r_2\\ \pi r_2^2, & r_2<r_1,\ d\leqslant r_1-r_2,\end{cases}$$

and where

$$x_i=\frac{R_t^2-R_c^2+r^2}{2r}.\tag{A5}$$

$$A_c=\begin{cases} 0, & R_t>R_c,\ r\leqslant R_t-R_c \\ 4R_t\displaystyle\int_0^{\sqrt{R_c^2-(R_t-r)^2}} \cos^{-1}\left(\frac{R_t^2-R_c^2+r^2+z^2}{2rR_t}\right)dz, & R_t>R_c,\ r>R_t-R_c \\ 4R_t\displaystyle\int_0^{\sqrt{R_c^2-(R_t-r)^2}} L_{\rm arc}(R_c,R_t,r)dz, & R_t\leqslant R_c, \end{cases} \tag{A6}$$

where

$$L_{\rm arc}(R_c,R_t,r)=\begin{cases} \cos^{-1}\left(\dfrac{R_t^2-R_c^2+r^2+z^2}{2rR_t}\right), & \begin{cases}\sqrt{R_c^2-z^2}<R_t+r,\\ \sqrt{R_c^2-z^2}>R_t-r\end{cases} \\ 0, & \begin{cases}\sqrt{R_c^2-z^2}<R_t+r,\\ \sqrt{R_c^2-z^2}\leqslant R_t-r\end{cases} \\ \pi, & \sqrt{R_c^2-z^2}\geqslant R_t+r. \end{cases} \tag{A7}$$

### 3. 0D spheres

$$V_c=\begin{cases} \frac{4}{3}\pi R_c^3, & R_c\leqslant R_t,\ r\leqslant R_t-R_c \\ \pi\left[\begin{array}{l}(R_c^2-r^2)(x_i-r+R_c)+r[x_i^2-(r-R_c)^2]- \\ \frac{1}{3}[x_i^3-(r-R_c)^3]+R_t^2(R_t-x_i)-\frac{1}{3}(R_t^3-x_i^3)\end{array}\right], & R_c\leqslant R_t,\ r>R_t-R_c \\ \frac{4}{3}\pi R_t^3, & R_c>R_t,\ r\leqslant R_c-R_t \\ \pi\left[\begin{array}{l}(R_c^2-r^2)(x_i-r+R_c)+r[x_i^2-(r-R_c)^2]- \\ \frac{1}{3}[x_i^3-(r-R_c)^3]+R_t^2(R_t-x_i)-\frac{1}{3}(R_t^3-x_i^3)\end{array}\right], & R_c>R_t,\ r>R_c-R_t, \end{cases} \tag{A8}$$

$$A_c=\begin{cases} 4\pi R_t^2, & R_c=R_t,\ r=0 \\ 4\pi R_t^2\sin^2\left[\frac{1}{2}\sin^{-1}\left(\dfrac{R_t^2-R_c^2+r^2}{2rR_t}\right)\right], & R_c=R_t,\ r>0 \\ 0, & R_c<R_t,\ r\leqslant R_t-R_c \\ 4\pi R_t^2\sin^2\left[\frac{1}{2}\sin^{-1}\left(\dfrac{R_t^2-R_c^2+r^2}{2rR_t}\right)\right], & R_c<R_t,\ r>R_t-R_c \\ 4\pi R_t^2, & R_c>R_t,\ r\leqslant R_c-R_t \\ 4\pi R_t^2\sin^2\left[\frac{1}{2}\sin^{-1}\left(\dfrac{R_t^2-R_c^2+r^2}{2rR_t}\right)\right], & R_c>R_t,\ r>R_c-R_t. \end{cases} \tag{A9}$$

*Current Address: Avionics Directorate, Wright Laboratory, Wright-Patterson AFB, OH 45433.

[1] M. J. Estes and G. Moddel, Appl. Phys. Lett. **68**, 1814 (1996).

[2] E. Bustarret, M. Ligeon, and L. Ortéga, Solid State Commun. **83**, 461 (1992).

[3] E. Bustarret, I. Mihalcescu, M. Ligeon, R. Romestain, J. C. Vial, and F. Madéore, J. Lumin. **57**, 105 (1993).

[4] S. Lazarouk, S. Katsuba, N. Kazuchits, G. D. Cesare, S. L. Monica, G. Maiello, E. Proverbio, and A. Ferrari, in *Microcrystalline and Nanocrystalline Semiconductors*, edited by L. Brus, M. Hirose, R. W. Collins, F. Koch, and C. C. Tsai, MRS Symposia Proceedings No. 358 (Materials Research Society, Pittsburgh, PA, 1994), p. 93.

[5] M. J. Estes, L. R. Hirsch, S. Wichart, and G. Moddel, presented at the *1996 Materials Research Society Spring Meeting, San Francisco, CA* (Materials Research Society, Pittsburgh, PA, 1996), paper A15.37.

[6] Z. N. Lu, D. J. Lockwood, and J.-M. Baribeau, Nature (London) **378**, 258 (1995).

[7] M. Estes, and G. Moddel, presented at *Spatial Light Modulators and Applications, Salt Lake City, UT* (Optical Society of America, Washington, DC, 1995).

[8] N. Noguchi, K. Suemune, M. Yamanishi, G. C. Jua, and N. Otsuka, Jpn. J. Appl. Phys. **31**, L490 (1992).

[9] J. M. Perez, J. Villalobos, P. McNeill, J. Prasad, R. Cheek, J. Kelber, J. P. Estrera, P. D. Stevens, and R. Glosser, Appl. Phys. Lett. **61**, 563 (1992).

[10] S. M. Prokes, J. J. A. Freitas, and P. C. Searson, Appl. Phys. Lett. **60**, 3295 (1992).

[11] R. E. Hollingsworth, M. J. Estes, C. DeHart, and P. K. Bhat,

presented at the *American Vacuum Society 41st National Symposium, Denver, CO* (American Vacuum Society, New York, 1994).
[12] N. Ookubo, J. Appl. Phys. **74**, 6375 (1993).
[13] P. N. Saeta, and A. C. Gallagher, in *Microcrystalline and Nanocrystalline Semiconductors* (Ref. 4), p. 981.
[14] Y. Kanemitsu, Phys. Rev. B **49**, 16 845 (1994).
[15] R. A. Street, in *Semiconductors and Semimetals*, edited by J. Pankove (Academic Press, New York, 1984), Vol. 21B, p. 197.
[16] L. T. Canham, Appl. Phys. Lett. **57**, 1046 (1990).
[17] Y. H. Seo, K. S. Nahm, M. H. An, E.-K. Suh, Y. H. Lee, K. B. Lee, and H. J. Lee, Jpn. J. Appl. Phys. **33**, 6425 (1994).
[18] R. Carius, R. Fischer, E. Hozenkämpfer, and J. Stuke, J. Appl. Phys. **52**, 4241 (1981).
[19] B. H. Augustine, E. A. Irene, Y. J. He, K. J. Price, L. E. McNeil, K. N. Christensen, and D. M. Maher, J. Appl. Phys. **78**, 4020 (1995).
[20] T. Tiedje, B. Abeles, and B. G. Brooks, Phys. Rev. Lett. **54**, 2545 (1985).
[21] T. Tiedje, in *Materials Issues in Applications of Amorphous Silicon Technology*, edited by D. Adler, A. Madan, and M. J. Thompson, MRS Symposia Proceedings No. 49 (Materials Research Society, Pittsburgh, PA, 1985), p. 121.
[22] M. Kemp, presented at the *1995 Materials Research Society Spring Meeting, San Francisco, CA* (Materials Research Society, Pittsburgh, PA, 1995), paper A3.1.
[23] D. J. Dunstan, and F. Boulitrop, Phys. Rev. B **30**, 5945 (1984).
[24] D. Adler, in *Physical Properties of Amorphous Materials*, edited by D. Alser *et al.* (Plenum, New York, 1985), p. 5.
[25] S. M. Prokes, J. Mater. Res. **11**, 305 (1996).
[26] M. S. Brandt, H. D. Fuchs, M. Stutzmann, J. Weber, and M. Cardona, Solid State Commun. **81**, 307 (1992).
[27] R. W. Collins, M. A. Paesler, and W. Paul, Solid State Commun. **34**, 833 (1980).
[28] R. A. Street, Adv. Phys. **30**, 593 (1981).
[29] J. von Behren, K. B. Ücer, L. Tsybeskov, J. V. Vandyshev, and P. M. Fauchet, J. Vac. Sci. Technol. B **13**, 1225 (1995).
[30] N. Mott, *Conduction in Non-Crystalline Materials* (Clarendon, Oxford, 1987), p. 27.